Supplementary Information (SI) for Energy & Environmental Science.

Supporting Information (SI) for

Revealing Heterogeneous Electric Double Layer (EDL) Structures of Localized High-Concentration Electrolytes (LHCE) and Their Impact on Solid-Electrolyte Interphase (SEI) Formation in Lithium Batteries

Qisheng Wu, and Yue Qi*
School of Engineering, Brown University, Providence, RI 02912, United States
*Corresponding author: Y. Q. (yueqi@brown.edu)

The DFT-MD-Data Modeling Methods

In this approach, molecular dynamics (MD) simulations were used to simulate the EDL structures based on the force field that calibrated with density functional theory (DFT) calculations. Then the data/statistical analysis were preformed to capture representative EDL building blocks and generate the input structures for DFT calculations. Finally, the DFT computed reduction votlages are combined with the data analysis results to give the sequence and probability of different reduced species that contribute to SEI formation.[1]

MD simulations of the EDL. All classical molecular dynamics simulations were carried out using the Forcite module in the BIOVIA Materials Studio (MS) 2020 software.[2] The COMPASS III force field[3] was employed with a charge scale of 0.7 for Li^+ and FSI^- to account for the polarizable effects. The calibration the force field vs. DFT calculations on the different interactions were provided in our recent publications.[1,4] The interfacial models for LCE, HCE, and LHCE were constructed following the approach described in our recent publication.[1] More specifically, the interfacial model consists of two graphene electrodes, the electrolyte, and a vacuum layer. The *x*- and *y*-dimensions of the simulation cells are 34.1 Å × 34.4 Å. The equilibrated electrolyte thickness is ~100.0 Å to ensure bulk electrolyte behavior in its center region.[5] The two graphene electrodes are negatively (left) and positively (right) charged and termed as anode and cathode, respectively. The length of the simulation box along the direction perpendicular to the electrode plane is around three times the electrolyte layer thickness to eliminate the artificial image effects from the periodic cells.[1,6] The number of LiFSI salt, DME solvent, and TFEO diluent in the interfacial systems for LCE(1-9), HCE(1-1.4), HCE(1-1.2), and LHCE(1-1.2-2) are given in **Table S1**. A constant charge method was used to apply extra charges to the graphene electrodes with several surface charge densities considered (σ=0.0, ±0.4, ±0.6, ±0.8, and ±1.2 e/nm^2). Note that σ=±0.6 e/nm^2 is about the surface charge at the electrochemical equilibrium condition for Li^+/Li^0.[7] After the equilibrated distance between the two graphene electrodes was determined under uncharged conditions (σ=0.0 e/nm^2) with a 0.2 ns simulation and an ensemble of constant number, volume, and temperature (NVT), the graphene electrodes were fixed for subsequent simulations. The interfacial systems were equilibrated for 2.0 ns under uncharged conditions and then for 8.0 ns under each charge density condition. Lastly, additional 8.0 ns simulations under each charge density condition were conducted and used for data analyses. The timestep was set to 2.0 fs with fixed bonds connected to hydrogen, and the temperature was set to 298 K for all simulations.

Data and Statistical analyses of the EDL. In this work, the EDL is defined as the region within 10.0 Å from the surface of the negatively charged graphene electrode.[8] Species were considered to be located within the EDL if any of the atoms of the species were in the EDL. Since the Li^+ coordination can increase the reduction voltage of a solvent species dramatically,[9] we analyzed the statistics of the electrolyte in the EDL in terms of a) solvents/anions coordinated with Li^+ in the first solvation shell and b) free solvent/anions species (not coordinated to any Li^+). Following our recent publication,[1] we used the one-electron reduction-center based counting for the onset of electrolyte reduction reactions. This means, each Li^+-coordinated cluster was counted as one and the number of each Li$^+$-coordinated clusters type, N_i, sums to the total number of Li$^+$ ions, $N_{Li} = \sum_i N_i$. A cutoff of 2.8 Å was used to define the first solvation shell of Li$^+$ ion. Each free specie was counted as one and the number of each specie type, N_j, sums to the total number of free species, $N_f = \sum_j N_j$. Thus, the SEI formation probability for each Li$^+$-coordinated cluster, *i*, is $P_i = N_i/(N_{Li} + N_f)$, while the SEI formation probability for each free specie, *j*, is calculated as $P_j = N_j/(N_{Li} + N_f)$.

DFT calculations. Density functional theory (DFT) calculations were conducted using the M06-2X[10] functional, the 6-31+G(d,p) basis set, and the D3 dispersion correction[11] as implemented in the Gaussian 09 code (version D.01)[12] following our previous work.[1] The SMD solvation model[13] was used to account for the solvation environment, and the dielectric constants were set to ε=7.2.[14] The reduction potential w.r.t. Li$^+$/Li^0 was calculated using the equation $E(vs\ Li/Li^+) = -\Delta G/F - 1.4$, where ΔG is the Gibbs free energy change and *F* is the Faraday constant.

In previous DFT-MD-data calculation protocol, only reduction voltages were computed.[1] In this new anyalsis, Marcus theory[15,16] was used to calculate the kinetics of reduction reactions. Specifically, it is assumed that all reduction reactions occur heterogeneously, with electrons transferred from the electrode.[17] The energy barrier ΔG^+ for a reduction reaction is

$$\Delta G^+ = \frac{\lambda}{4}[1 + \frac{\Delta G^0}{\lambda}]^2 \tag{4}$$

where ΔG^0 is the Gibbs free energy and λ is the reorganization energy, which can be decomposed into the inner-shell reorganization energy λ_{in} and a bulk outer-shell reorganization energy λ_{out} ($\lambda = \lambda_{in} + \lambda_{out}$). The four-point method of Nelsen[18] is used to approximate the inner-shell electron reorganization energy, while Marcus's expression is used for the outer-shell term[17,19]:

$$\lambda_{out} = \frac{(\Delta e)^2}{8\pi\varepsilon_0}\left(\frac{1}{r} - \frac{1}{2D}\right)\left(\frac{1}{\varepsilon} - \frac{1}{\varepsilon_s}\right) \tag{5}$$

where Δe is the transferred electron (that is *e* for each one-electron reduction reaction), ε_0 is the vacuum permittivity (8.85 × 10^{-12} F/m), r is the radius of the reacting molecule and its first solvation shell (all assumed to be 5.0 Å for simplicity)[19], *D* is the molecule-electrode distance (set to 5.0 Å for calculating λ_{out}), ε is the optical dielectric constant (~2.0)[19] and ε_s is the static dielectric constant (taken to be 20.5)[20,21]. The calculation results of all the reactions are listed in Figure 7, Figure S16 and Table S2.

Table S1. List of the number of species (LiFSI, DME, and TFEO) in the interfacial systems of LCE(1-9), HCE (1-1.4), HCE(1-1.2), and LHCE(1-1.2-2).

System	**LCE(1-9)**	**HCE(1-1.4)**	**HCE(1-1.2)**	**LHCE(1-1.2-2)**
LiFSI	72	330	360	120
DME	648	462	432	144
TFEO	/	/	/	240

Table S2. List of the Gibbs free energy change (ΔG^0), inner-shell reorganization energy (λ_{in}), outer-shell reorganization energy (λ_{out}), and total reorganization energy (λ) for all the reduction reactions shown in Figure 7 and Figure S16.

Reduction reaction source	ΔG^0 (eV)	λ_{in} (eV)	λ_{out} (eV)	λ (eV)
Figure 7a	-2.244	2.605	0.324	2.929
Figure 7b	-4.106	3.328	0.324	3.652
Figure 7c	-0.389	2.764	0.324	3.089
Figure 7d	-2.034	2.632	0.324	2.956

Figure 7e	-1.607	3.219	0.324	3.543
Figure 7f	-3.248	3.168	0.324	3.492
Figure S16a	-0.148	3.178	0.324	3.502
Figure S16c	-2.189	3.718	0.324	4.042
Figure S16c	-3.79	1.449	0.324	1.773

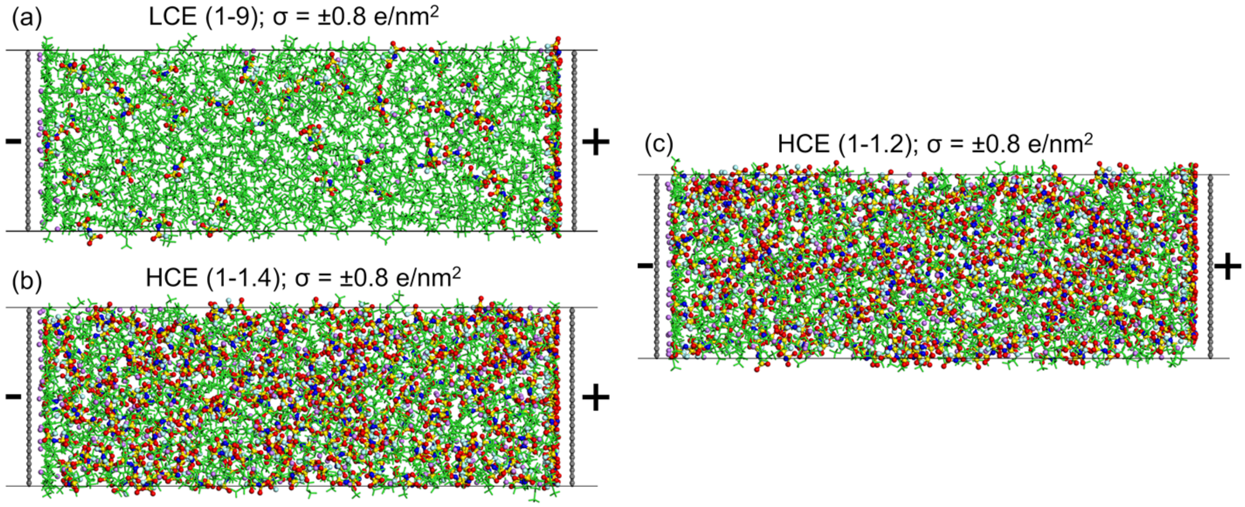

Figure S1. Final frames of the MD trajectories for (a) LCE(1-9), (b) HCE (1-1.4), and (c) HCE(1-1.2) under the graphene surface charge density of σ=±0.8 e/nm^2.

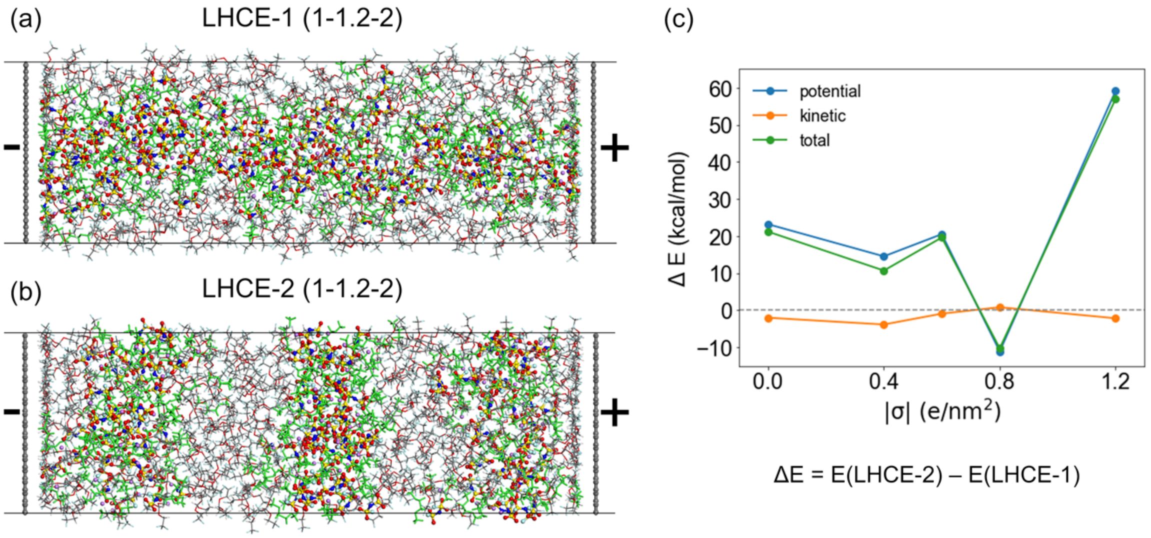

Figure S2. Initial configurations for (a) LHCE-1(1-1.2-2) and (b) LHCE-2(1-1.2-2). (c) Time-averaged potential, kinetic, and total energy differences between LHCE-1 and LHCE-2 under different surface charge densities of the graphene electrode during the last 8.0 NVT simulations.

It is seen that the total energy differences fluctuate between small positive and negative values depending on the surface charge density of the graphene electrode, suggesting both scenarios would occur in real interfacial systems.

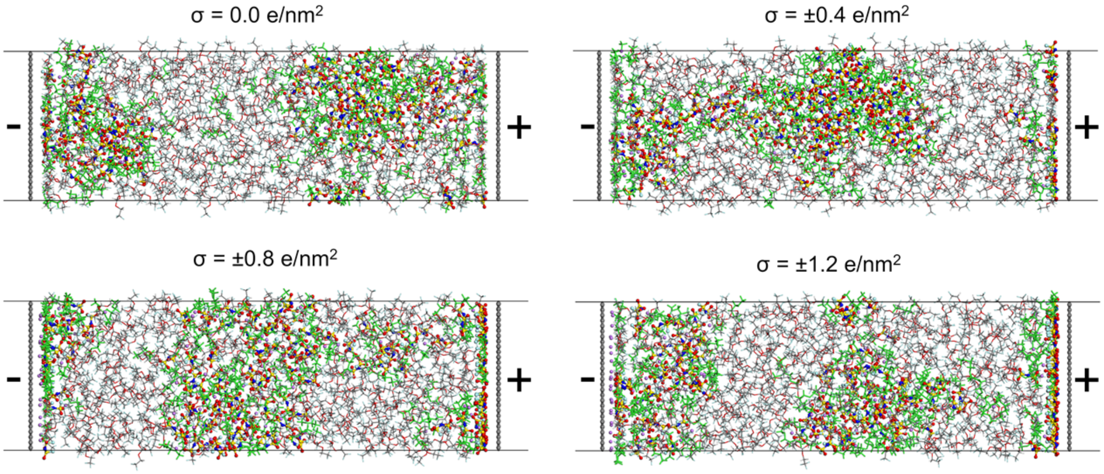
σ = 0.0 e/nm²

σ = ±0.4 e/nm²

σ = ±0.8 e/nm²

σ = ±1.2 e/nm²

Figure S3. Simulated structures of LHCE-1 (1-1.2-2) under surace charge densities of σ=0.0 e/nm^2, ±0.4 e/nm^2, ±0.8 e/nm^2, and ±1.2 e/nm^2. The simulated structure that corresponds to σ=±0.6 e/nm^2 is shown in the main text.

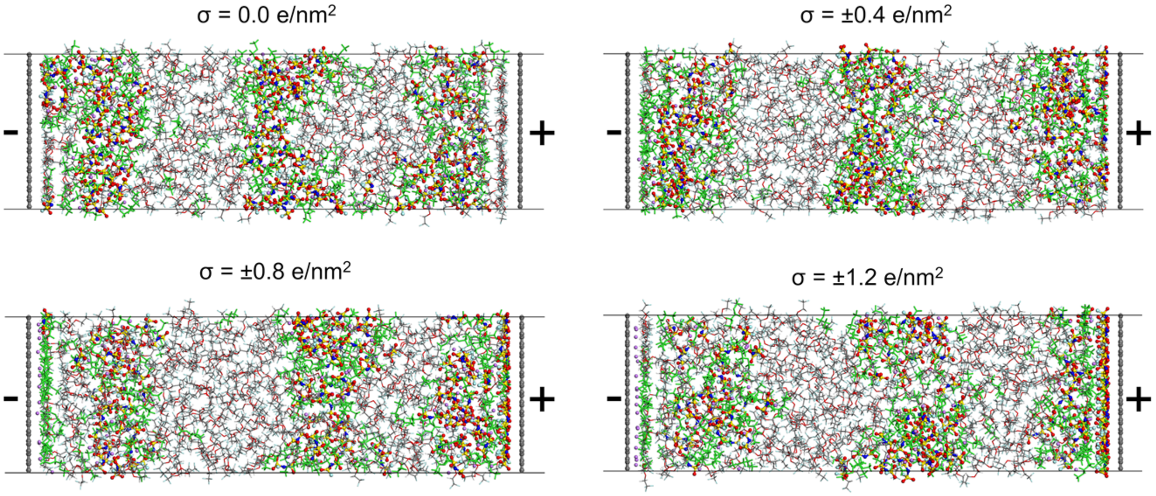
σ = 0.0 e/nm²

σ = ±0.4 e/nm²

σ = ±0.8 e/nm²

σ = ±1.2 e/nm²

Figure S4. Simulated structures of LHCE-2 (1-1.2-2) under surace charge densities of σ=0.0 e/nm^2, ±0.4 e/nm^2, ±0.8 e/nm^2, and ±1.2 e/nm^2. The simulated structure that corresponds to σ=±0.6 e/nm^2 is shown in the main text.

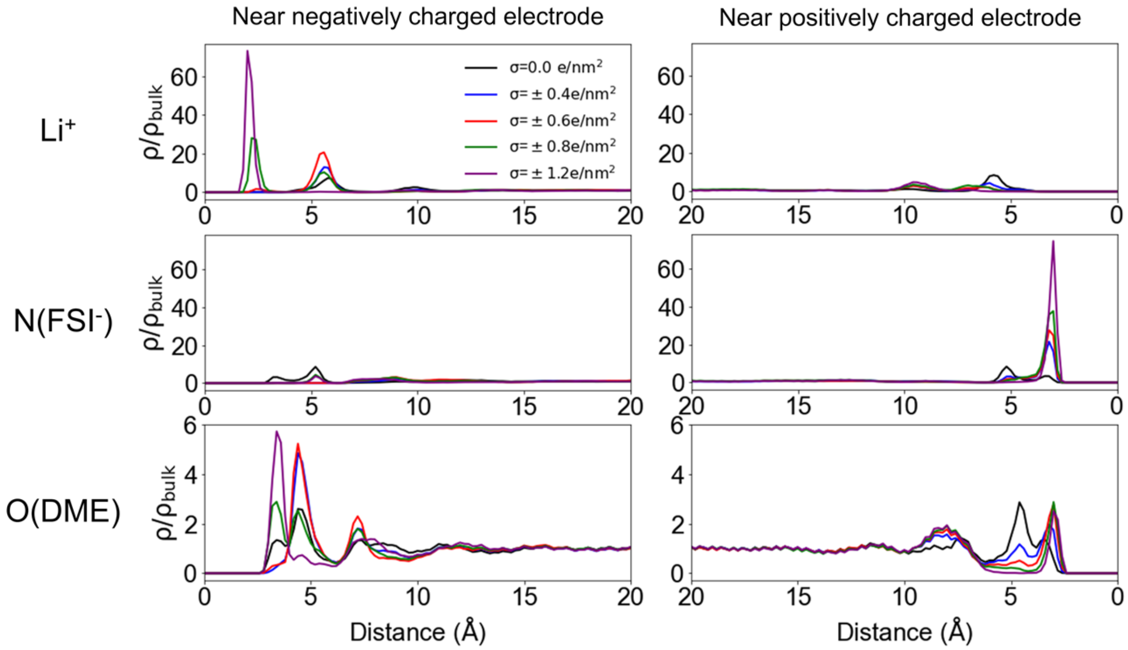

Figure S5. Normalized number density profiles of Li^+ , FSI^- and DME for the LCE(1-9) electrolyte under different charge densities for the graphene electrode. N and O atoms are used for representing FSI^- and DME, respectively.

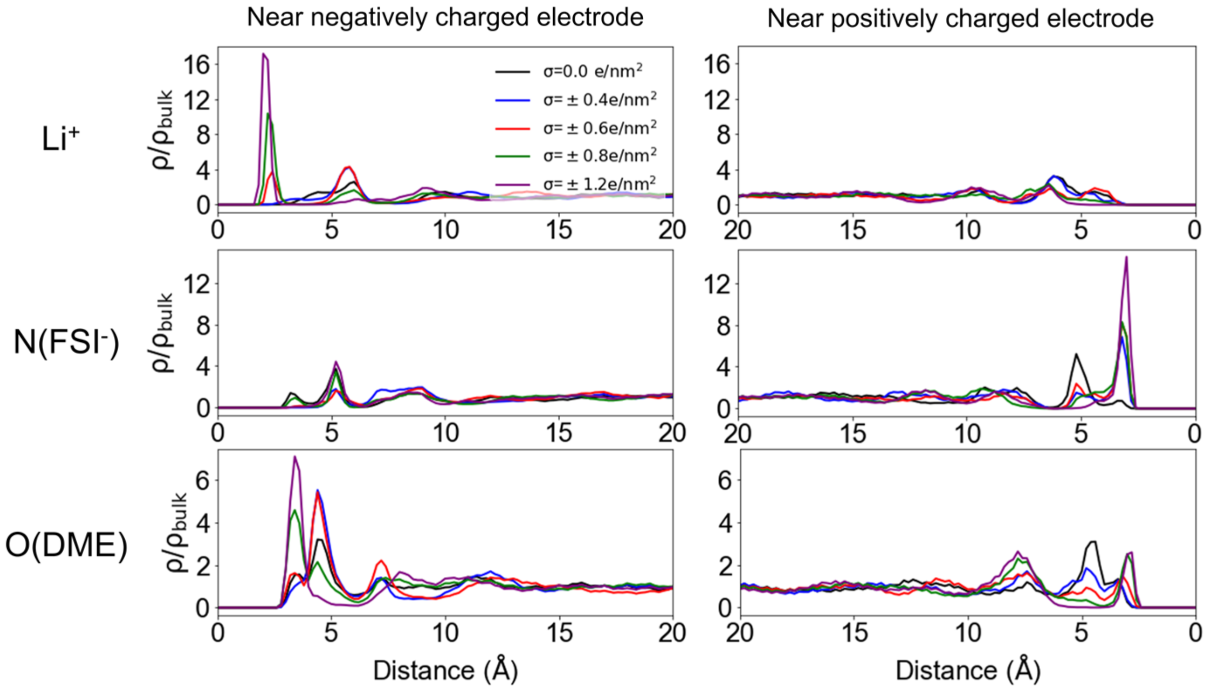

Figure S6. Normalized number density profiles of Li^+, FSI^-, and DME for the HCE(1-1.4) electrolyte under different charge densities for the graphene electrode. N and O atoms are used for representing FSI^- and DME, respectively.

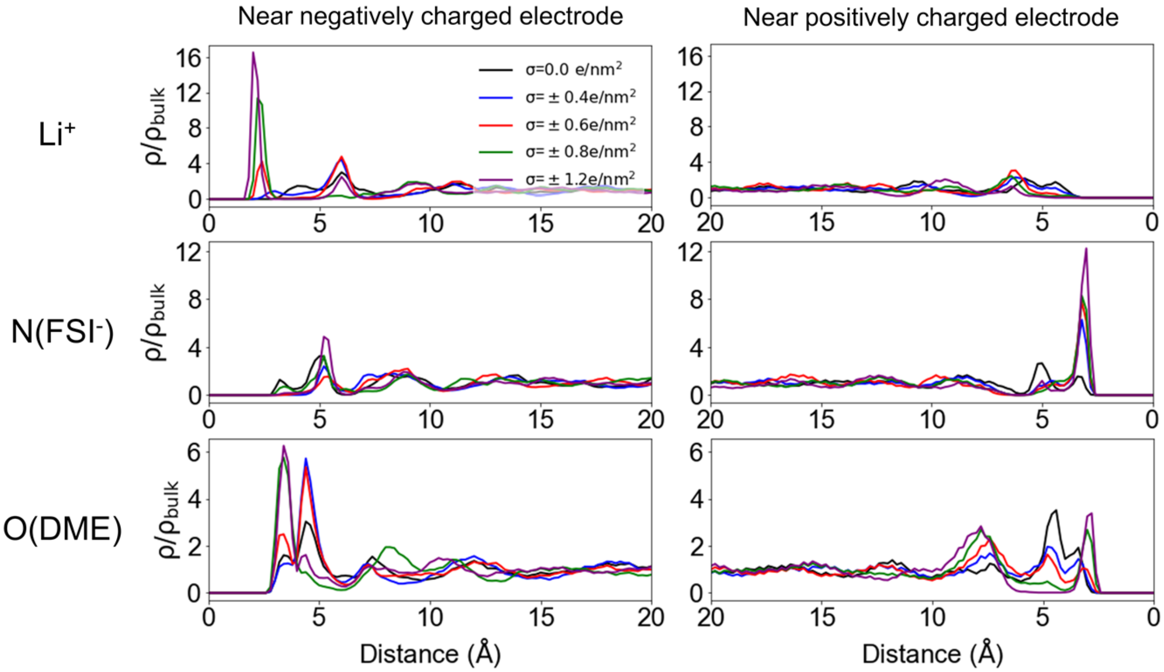

Figure S7. Normalized number density profiles of Li^+, FSI^-, and DME for the HCE(1-1.2) electrolyte under different charge densities for the graphene electrode. N and O atoms are used for representing FSI^- and DME, respectively.

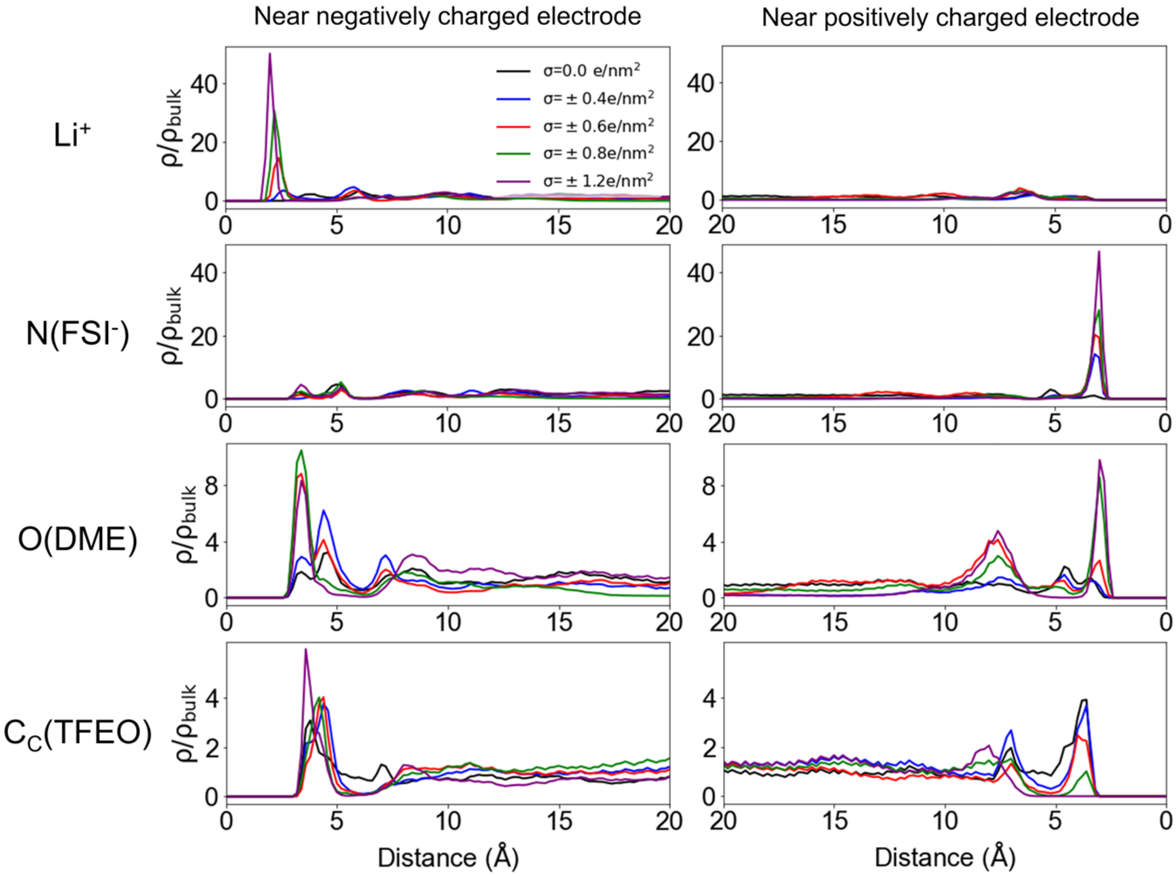

Figure S8. Normalized number density profiles of Li^+, FSI^-, DME, and TFEO for the LHCE-1(1-1.2-2) electrolyte under different charge densities for the graphene electrode. N and O atoms are used for representing FSI^- and DME, respectively. The center C atom (C_C) is used for representing TFEO.

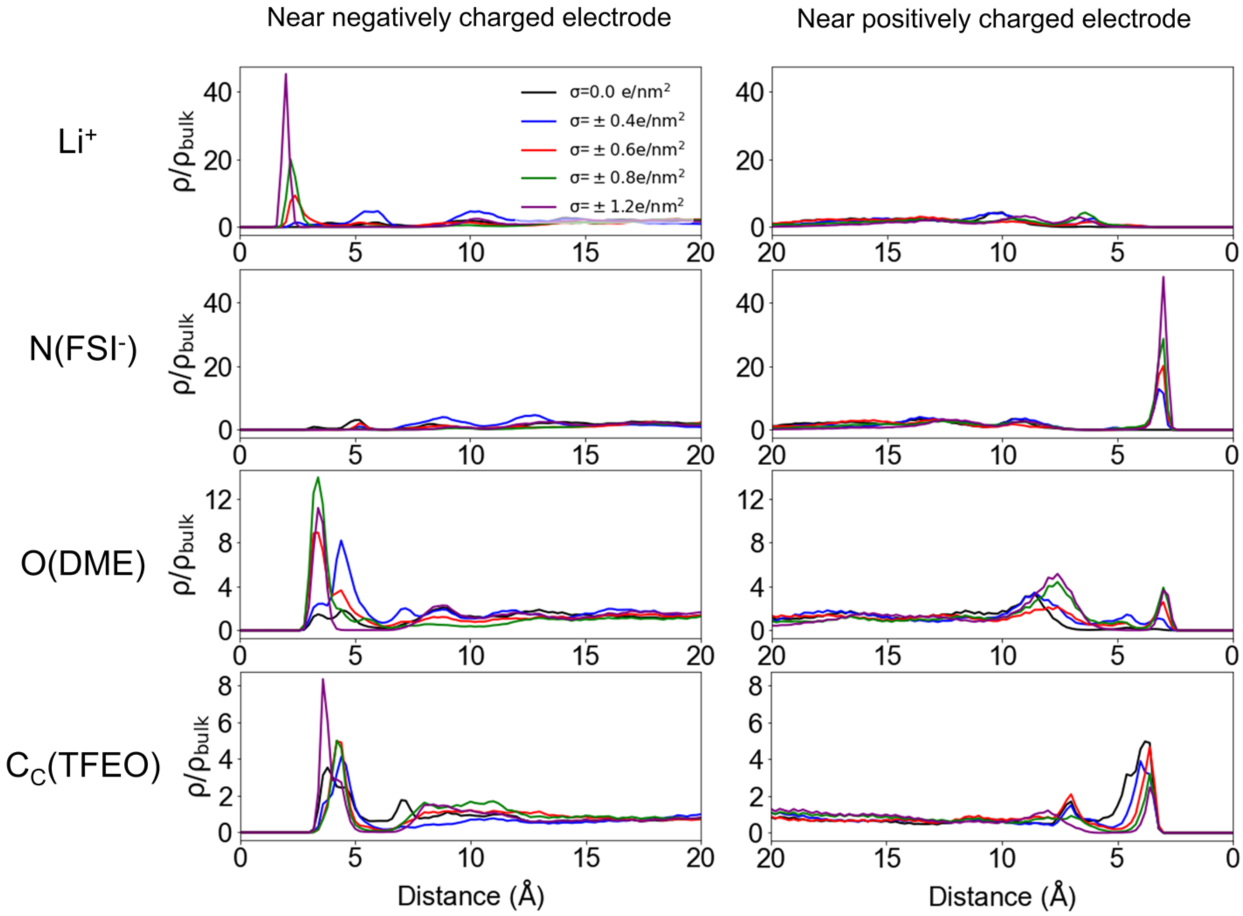

Figure S9. Normalized number density profiles of Li^+, FSI^-, DME, and TFEO for the LHCE-2(1-1.2-2) electrolyte under different charge densities for the graphene electrode. N and O atoms are used for representing FSI^- and DME, respectively. The center C atom (C_C) is used for representing TFEO.

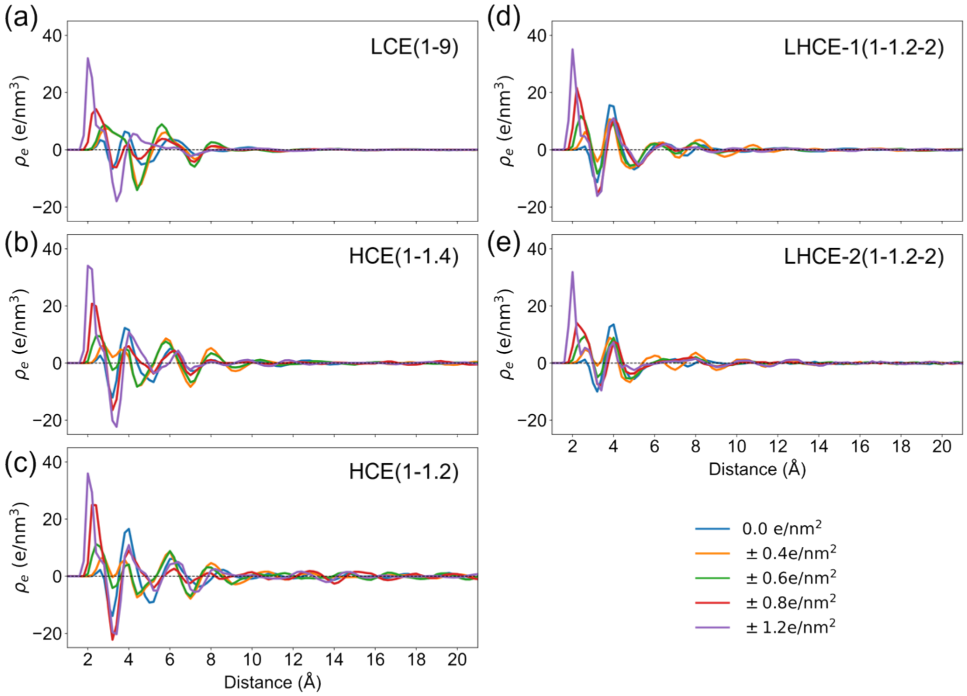

Figure S10. Charge density profiles near the negatively charged graphene electrode under different surface charge densities for (a) LCE(1-9), (b) HCE(1-1.4), (c) HCE(1-1.2), (d) LHCE-1(1-1.2-2), and (e) LHCE-2(1-1.2-2).

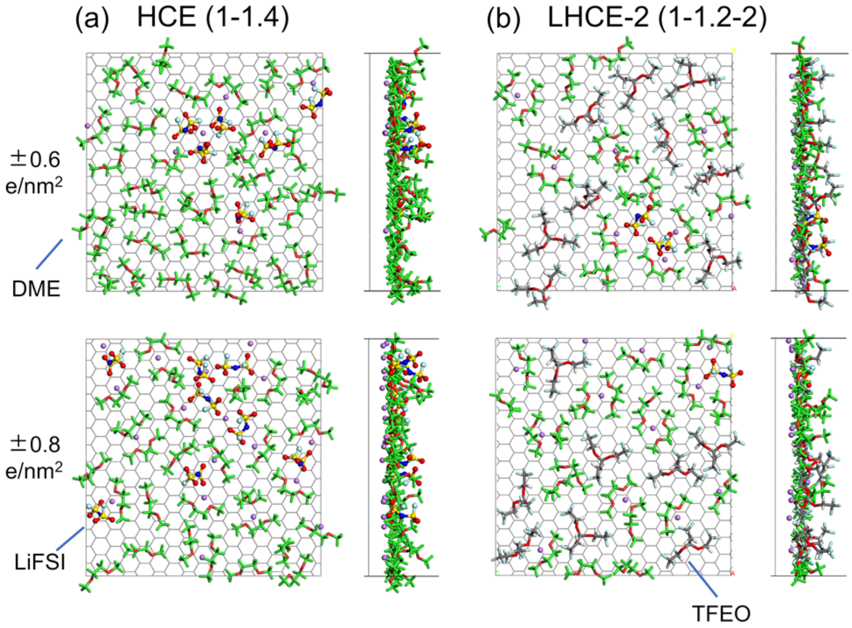

Figure S11. Snapshots of the interfacial structures of directly adsorbed electrolye species for HCE(1-1.4) and LHCE-2 (1-1.2-2) systems under graphene electrode surface charge densities of σ=±0.6 e/nm^2 and σ=±0.8 e/nm^2. The DME molecules are represented with green stick models but the oxygen atoms in DME are highlighted with red for clarity.

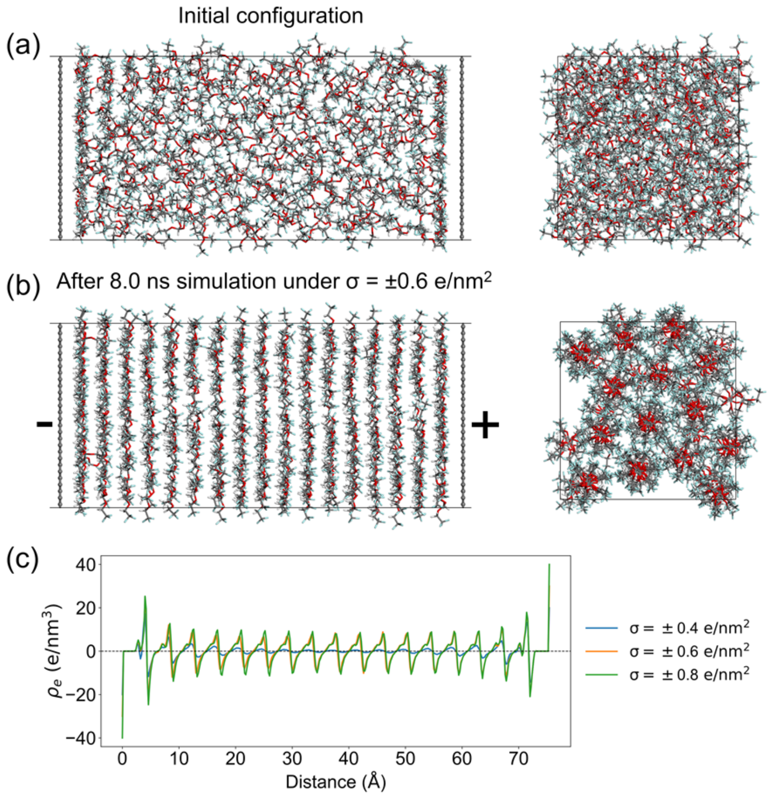

Figure S12. Simulations of pure TFEO system sandwiched by two charged graphene electrodes. (a) Initial configuration (left: side view; right: top view). (b) The TFEO system after 8.0 ns NVT simulation under σ=±0.6 e/nm^2 (left: side view; right: top view). It is seen that TFEO forms layered structures with hydrogen pointing toward the negatively charged graphene electrode and fluorine pointing toward the positively charged graphene electrode. (c) Charge density distributions as functions of distance from the negatively charged graphene electrode for the last 4.0 ns NVT simulations under different surface charge densities of the graphene electrode. The system contains 240 TFEO molecules, and the distance between the graphene electrodes is fixed to be 75.4 Å.

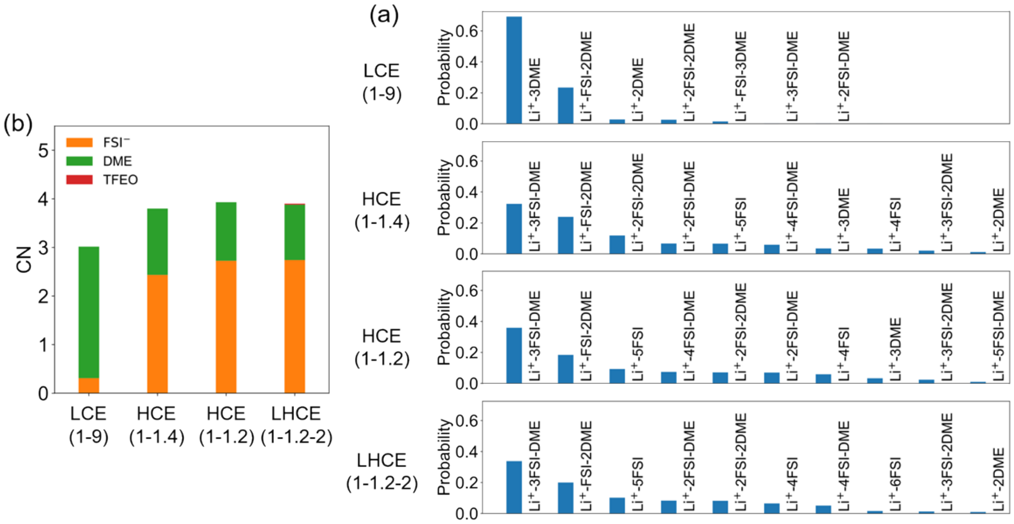

Figure S13. (a) Averaged coordination numbers of Li^+ to FSI^-, DME, and TFEO in the bulk phases of LCE(1-9), HCE(1-1.4), HCE(1-1.2), and LHCE(1-1.2-2). (b) Probability distributions of the solvation structures of the first solvation shell of Li^+ ions in the bulk phase of LCE(1-9), HCE(1-1.4), HCE(1-1.2), and LHCE(1-1.2-2) electrolytes. For example, "FSI-2DME" refers to that Li^+ is coordinated with one FSI^- and two DME molecules. Only ten solvation shell structures with the highest probabilities are shown for each electrolyte. Statistics are obtained based on the data reported in our recent publication.[4]

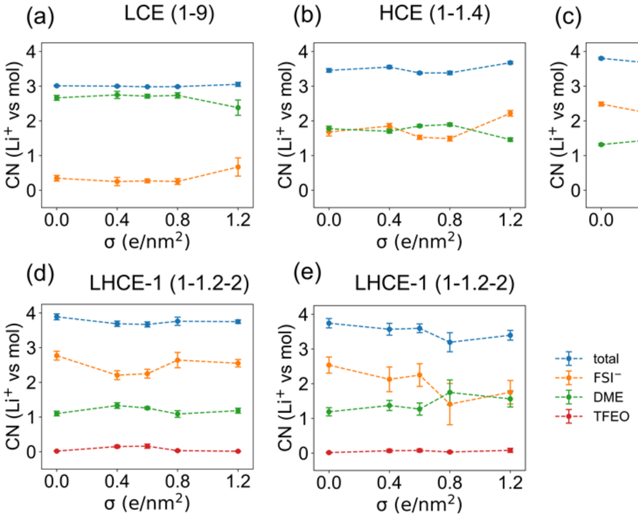

Figure S14. Coordination numbers between the second-layer Li^+ ions in the EDL (5.0-10.0 Å from the negatively charged graphene electrode) and other species (FSI^-, DME, and TFEO) under different surface charge densities of graphene electrode.

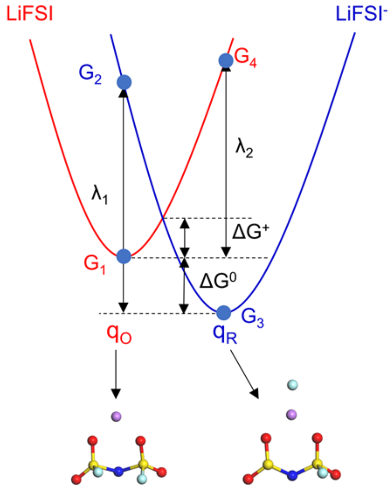

Figure S15. Scheamtic of the four-point method of Nelsen[18] for calculating Gibbs free energy change (ΔG^0) and reaction barrier (ΔG^+). Here the reduction of LiFSI is shown as an example: LiFSI + e^- → $LiFSI^-$. See methods section in SI for more calculation details.

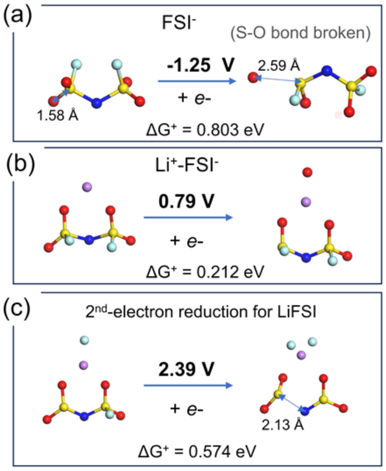

Figure S16. Reduction reaction calculation for (a) FSI$^-$ and (b) LiFSI with broken S-O bond. (c) Calculation of the 2nd-electron reduction for LiFSI. Both reduction voltages (with respect to Li/Li$^+$) and reduction reaction barriers are shown.

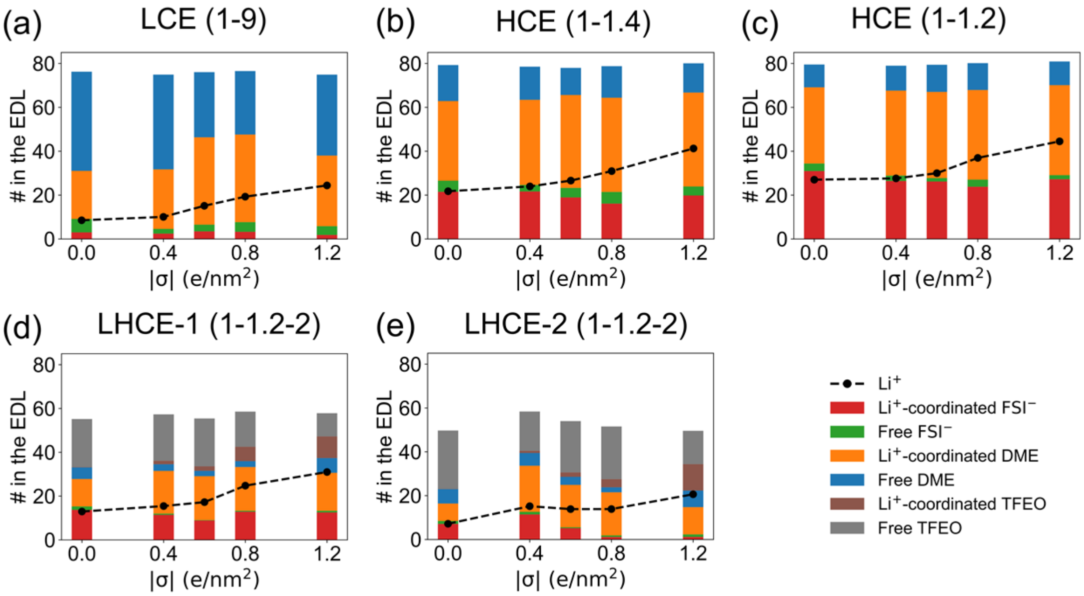

Figure S17. Number of species (Li$^+$, FSI$^-$, DME, and TFEO) in the EDL for the (a) LCE(1-9), (b) HCE(1-1.4), (c) HCE(1-1.2), (d) LHCE-1(1-1.2-2), and (e) LHCE-2(1-1.2-2) electrolyte systems.

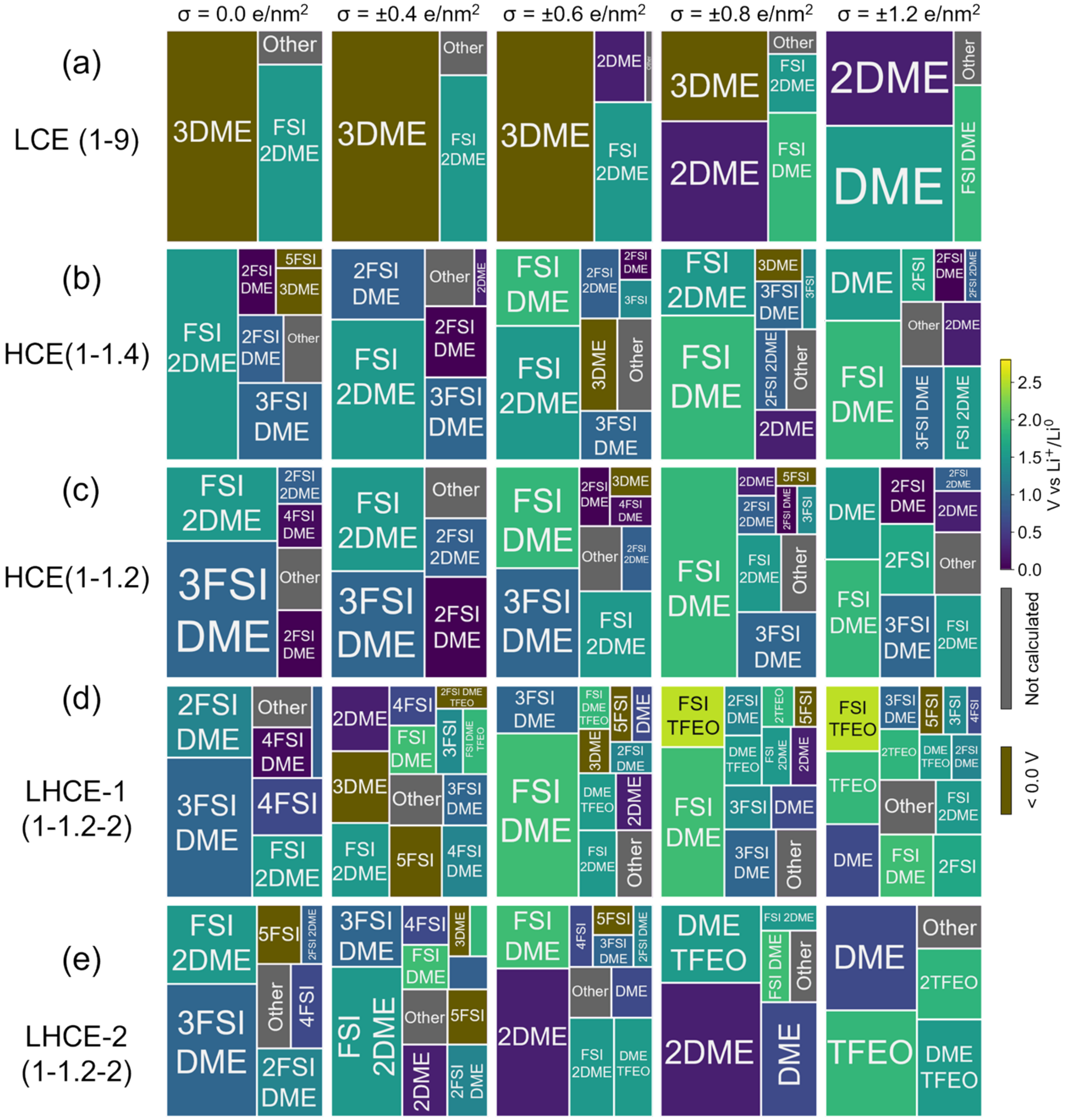

Figure S18. Probability distributions of the solvation structures in the first solvation shell of Li^+ ions within the EDL (10.0 Å from the negatively charged graphene electrode) under different graphene electrode charge densities: (σ = 0.0, ±0.4, ±0.6, ±0.8 and ±1.2 e/nm^2) for the (a) LCE(1-9), (b) HCE(1-1.4), (c) HCE(1-1.2), (d) LHCE-1(1-1.2-2) and (e) LHCE-2(1-1.2-2) electrolytes. Those solvation shell structures with the highest probabilities that accumulate up to 90% are shown with their reduction potentials (indicated by color coding), while the rest is labeled with "Other" (in gray).

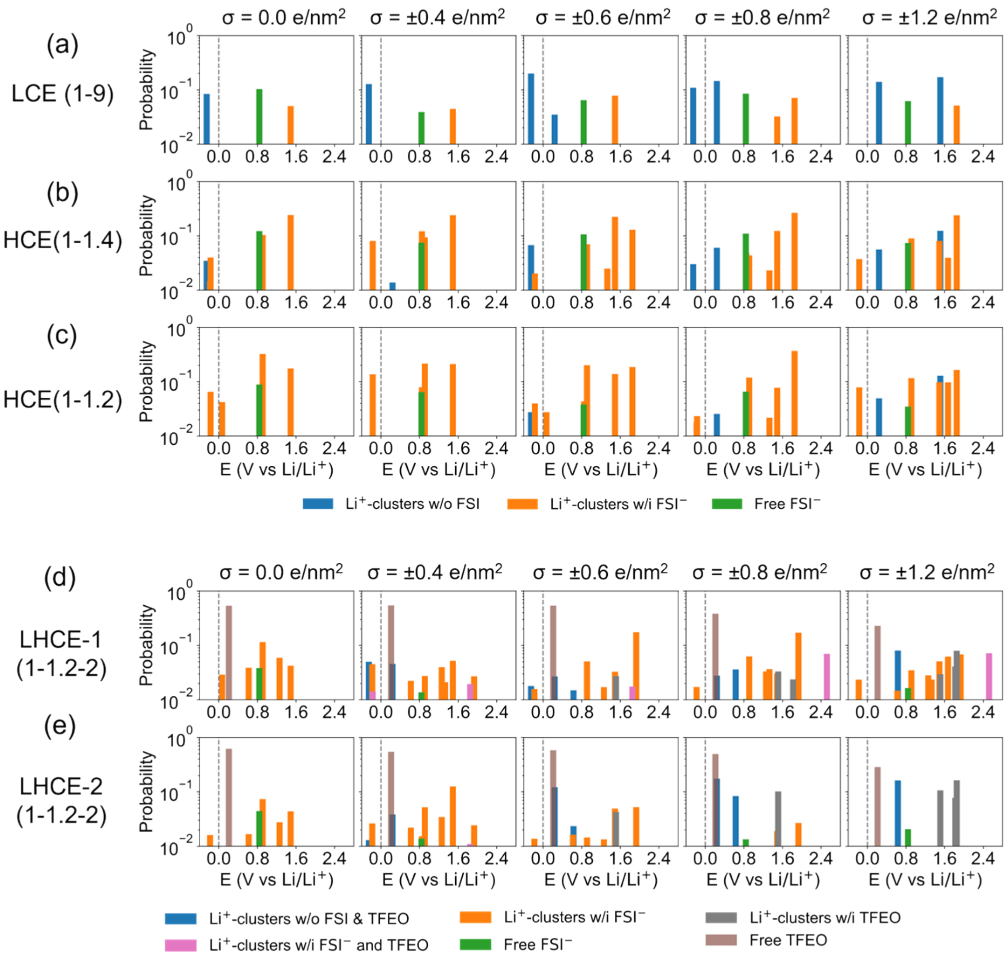

Figure S19. Probabilities in logscale of DFT-calculated reduction potentials for (a) LCE(1-9), (b) HCE(1-1.4), (c) HCE(1-1.2), (d) LHCE-1(1-1.2-2) and (e) LHCE-2(1-1.2-2) electrolytes under different surface charge densities of the graphene electrode. Contributions from different clusters and species are color-encoded, including Li^+-coordinated clusters with or without FSI^- as well as free FSI^-. Free DME has a negative reduction potential of -1.01 V *vs* Li/Li^+,[1] and is not shown in this figure.

References:

[1] Wu, Q.; McDowell, M. T.; Qi, Y. Effect of the Electric Double Layer (EDL) in Multicomponent Electrolyte Reduction and Solid Electrolyte Interphase (SEI) Formation in Lithium Batteries. *J Am Chem Soc* **2023**, *145* (4), 2473–2484.

[2] Dassault Systèmes BIOVIA, Materials Studio, 2020, San Diego: Dassault Systèmes, 2020.

[3] Akkermans, R. L. C.; Spenley, N. A.; Robertson, S. H. COMPASS III: Automated Fitting Workflows and Extension to Ionic Liquids. *Mol Simul* **2021**, *47* (7), 540–551.

[4] Efaw, C. M.; Wu, Q.; Gao, N.; Zhang, Y.; Zhu, H.; Gering, K.; Hurley, M. F.; Xiong, H.; Hu, E.; Cao, X.; et al. Localized High-Concentration Electrolytes Get More Localized through Micelle-like Structures. *Nat Mater* **2023**, *22* (12), 1531–1539.

[5] Rakov, D.; Hasanpoor, M.; Baskin, A.; Lawson, J. W.; Chen, F.; Cherepanov, P. V; Simonov, A. N.; Howlett, P. C.; Forsyth, M. Stable and Efficient Lithium Metal Anode Cycling through Understanding the Effects of Electrolyte Composition and Electrode Preconditioning. *Chemistry of Materials* **2022**, *34* (1), 165–177.

[6] Yeh, I. C.; Berkowitz, M. L. Ewald Summation for Systems with Slab Geometry. *Journal of Chemical Physics* **1999**, *111* (7), 3155–3162.

[7] Li, Y.; Qi, Y. Energy Landscape of the Charge Transfer Reaction at the Complex Li/SEI/Electrolyte Interface. *Energy Environ Sci* **2019**, *12* (4), 1286–1295.

[8] Abbott, J. W.; Hanke, F. Kinetically Corrected Monte Carlo–Molecular Dynamics Simulations of Solid Electrolyte Interphase Growth. *J Chem Theory Comput* **2022**, *18* (2), 925–934.

[9] Borodin, O.; Olguin, M.; Spear, C. E.; Leiter, K. W.; Knap, J. Towards High Throughput Screening of Electrochemical Stability of Battery Electrolytes. *Nanotechnology* **2015**, *26* (35), 354003.

[10] Zhao, Y.; Truhlar, D. G. The M06 Suite of Density Functionals for Main Group Thermochemistry, Thermochemical Kinetics, Noncovalent Interactions, Excited States, and Transition Elements: Two New Functionals and Systematic Testing of Four M06-Class Functionals and 12 Other Function. *Theor Chem Acc* **2008**, *120* (1–3), 215–241.

[11] Grimme, S.; Ehrlich, S.; Goerigk, L. Effect of the Damping Function in Dispersion Corrected Density Functional Theory. *J Comput Chem* **2011**, *32* (7), 1456–1465.

[12] M. J. Frisch, G. W. Trucks, H. B. Schlegel, G. E. Scuseria, M. A. Robb, J. R. Cheeseman, G. Scalmani, V. Barone, G. A. Petersson, H. Nakatsuji, X. Li, M. Caricato, A. Marenich, J. Bloino, B. G. Janesko, R. Gomperts, B. Mennucci, H. P. Hratchian, J. V. Ort, and D. J. F. Gaussian 09, Revision D.01. Gaussian, Inc.: Wallingford CT 2016.

[13] Marenich, A. V.; Cramer, C. J.; Truhlar, D. G. Universal Solvation Model Based on Solute Electron Density and on a Continuum Model of the Solvent Defined by the Bulk Dielectric Constant and Atomic Surface Tensions. *J Phys Chem B* **2009**, *113* (18), 6378–6396.

[14] Oehme, K.-L. Static Dielectric Constants of Pure Liquids and Binary Liquid Mixtures. *Zeitschrift für Physikalische Chemie* **1994**, *185* (2), 276–277.

[15] Marcus, R. A. Electron Transfer Reactions in Chemistry. Theory and Experiment. *Rev Mod Phys* **1993**, *65* (3), 599–610.

[16] Silverstein, T. P. Marcus Theory: Thermodynamics CAN Control the Kinetics of Electron Transfer Reactions. *J Chem Educ* **2012**, *89* (9), 1159–1167.

[17] Marcus, R. A. On the Theory of Electron-Transfer Reactions. VI. Unified Treatment for Homogeneous and Electrode Reactions. *J Chem Phys* **1965**, *43* (2), 679–701.

[18] Nelsen, S. F.; Blackstock, S. C.; Kim, Y. Estimation of Inner Shell Marcus Terms for Amino Nitrogen Compounds by Molecular Orbital Calculations. *J Am Chem Soc* **1987**, *109* (3), 677–682.

[19] Spotte-Smith, E. W. C.; Kam, R. L.; Barter, D.; Xie, X.; Hou, T.; Dwaraknath, S.; Blau, S. M.; Persson, K. A. Toward a Mechanistic Model of Solid–Electrolyte Interphase Formation and Evolution in Lithium-Ion Batteries. *ACS Energy Lett* **2022**, *7* (4), 1446–1453.

[20] Borodin, O.; Behl, W.; Jow, T. R. Oxidative Stability and Initial Decomposition Reactions of Carbonate, Sulfone, and Alkyl Phosphate-Based Electrolytes. *The Journal of Physical Chemistry C* **2013**, *117* (17), 8661–8682.

[21] Hall, D. S.; Self, J.; Dahn, J. R. Dielectric Constants for Quantum Chemistry and Li-Ion Batteries: Solvent Blends of Ethylene Carbonate and Ethyl Methyl Carbonate. *Journal of Physical Chemistry C* **2015**, *119* (39), 22322–22330.